POLITECNICO DI TORINO
Repository ISTITUZIONALE

Transient Overload Characteristics of PM-Assisted Synchronous Reluctance Machines, Including Sensorless Control Feasibility

Original
Transient Overload Characteristics of PM-Assisted Synchronous Reluctance Machines, Including Sensorless Control Feasibility / Leuzzi, R., Cagnetta, P., Ferrari, S., Pescetto, P., Pellegrino, G., Francesco, C.. - In: IEEE TRANSACTIONS ON INDUSTRY APPLICATIONS. - ISSN 0093-9994. - 55:3(2019), pp. 2637-2648. [10.1109/TIA.2019.2897969]

Availability:
This version is available at: 11583/2724386 since: 2019-07-04T17:23:01Z

Publisher:
IEEE

Published
DOI:10.1109/TIA.2019.2897969

Terms of use:

This article is made available under terms and conditions as specified in the corresponding bibliographic description in the repository

Publisher copyright

(Article begins on next page)

19 November 2026

Transient Overload Characteristics of PM-Assisted Synchronous Reluctance Machines, Including Sensorless Control Feasibility

R. Leuzzi, P. Cagnetta, S. Ferrari, P. Pescetto, G. Pellegrino, F. Cupertino

***Abstract*— Synchronous reluctance machines are a high-efficiency alternative to induction motors for variable-speed applications. To mitigate the well-known downside of their lower power factor, permanent-magnet-assisted topologies, in which either rare-earth or ferrite magnets are inserted into the rotor in suitable quantities, are often adopted. The design and optimization procedures for PM-assisted topologies have been thoroughly discussed in the related literature. This paper compares synchronous reluctance machines assisted with NdFeB and ferrite magnets, focusing on torque overload capability and feasibility of saliency-based position estimation algorithms. Three prototypes were realized and tested. They all have the stator of a commercial induction motor and the same custom-designed synchronous reluctance rotor laminations. Of the three prototypes, one is a pure synchronous reluctance motor, and the other two have NdFeB and ferrite magnets, respectively; both are designed to give the same torque at rated current. Results from simulations and experiments are presented comparing the transient overload capability of the three machines, in terms of torque capability and de-magnetization limit. A dynamic thermal model of the machines was developed within this scope. Moreover, the feasibility of saliency-based sensorless methods was investigated and is presented here for the three machines, both at high- and low-current loads. The results of the paper suggest that the ferrite-assisted solution is the best candidate for replacing induction motors in variable-speed applications, for its optimal tradeoff between performance and cost.**

***Index Terms*—demagnetization, high-frequency voltage injection, overload, permanent magnet motor, sensorless control, synchronous reluctance motor.**

I. INTRODUCTION[1]

SYNCHRONOUS reluctance (SyR) machines are gaining increasing interest in variable-speed industrial applications due to their low cost and high efficiency. Synchronous reluctance machines are more efficient and more compact than induction machines (IMs) with the same continuous torque rating, mainly due to the absence of the rotor cage and related losses in SyR machines [1]. Moreover, the transient overload capability is very high in SyR machines due to the absence of magnets, leading to peak torque values comparable to those of permanent-magnet synchronous machines.

Regarding the design of SyR machines, the maximization of magnetic saliency plays a critical role both in torque and power factor figures [2], [3], and constant power speed range, as described in [4]. Torque ripple is another main concern for the designers. It is demonstrated in the literature that if proper design measures are taken [5] and barrier shape optimization is performed [6], torque ripple can be drastically mitigated. If needed by the application, skewing the rotor is also an effective measure to eliminate residual torque oscillations, as is commonly done for IMs.

The insertion of permanent magnets (PMs) inside the rotor flux barriers produce an additional flux linkage component and, consequently, an additional torque contribution [7] and a larger constant power region [8]. Moreover, the PMs saturate the structural ribs of the rotor, with the advantages in zero current sensorless control described later. The final machine is defined as a PM-assisted machine, meaning that the main torque contribution remains the reluctance torque component. PM-assistance can be obtained using relatively small quantity of NdFeB magnets or larger quantity of ferrite magnets. Ferrites are very common and inexpensive iron oxides. They can tolerate temperatures up to 250°C or 300°C, which is well compatible to harsh environments. Furthermore, their coercivity increases with temperature, making them stronger toward demagnetization. Conversely, neodymium magnets are much stronger towards demagnetization, due higher nominal coercivity, but its maximum operating temperatures is around 120°C, unless dysprosium is added, with a notable cost increase. Designers and manufacturers have increasingly investigated the use of Dy-less [24] and ferrite magnets [25-26] in recent years, focusing mainly on the magnetic design and less on the thermal aspects.

This work extends the results shown in conference papers [9] and [14]. This paper compares one SyR motor and two PM-assisted SyR (PM-SyR) motors, using ferrite (ferrite-SyR) and NdFeB magnets (Neo-SyR), in terms of their overload capability, including the analysis of thermal transients and robustness toward irreversible demagnetization.

This work was supported in part by the Italian Ministry of University and Research under Grant PON03PE_00067_8.

R. Leuzzi, P. Cagnetta, and F. Cupertino are with the Department of Electrical and Information Engineering, Politecnico di Bari, Bari, Italy (e-mail: riccardo.leuzzi@poliba.it).

S. Ferrari, P. Pescetto, and G. Pellegrino are with the Department of Energy, Politecnico di Torino, Torino, Italy (e-mail: gianmario.pellegrino@polito.it).

Moreover, the paper presents a comparative analysis of the influence of the rotor type on saliency-based position detection. With respect to [9] and [14], the original contribution of this paper is the in-depth transient thermal analysis, leading to transient overload characteristics of the three machines. It is commonly known that the anisotropy of SyR motors is desirable also for the implementation of saliency-based sensorless control. Saliency is exploited in the low-speed range to estimate rotor position by adding high-frequency signals to the control voltages [10]. The position tracking accuracy is a function of machine design and loading conditions, and is investigated in the paper. A detailed explanation of the HF sensorless techniques is made in [11] and [12], where also the influence of the rotor structure on saliency and cross-coupling is considered. An in-depth investigation of cross-coupling effects for transverse-laminated SyR machines can also be found in [13]. The results of the paper show that the PM-assistance makes the sensorless control more insensitive to the operating point, avoiding the loss of saliency around zero torque, zero current conditions, typical of the pure SyR machine [17]. Moreover, the paper shows that the use of ferrite magnets is recommended for industry applications, both for its lower cost and its higher overall performance.

II. Design of the Three Machines

The three SyR prototypes that are analyzed in this paper were designed using a multi-objective optimization algorithm, starting from a commercial induction motor for general-purpose applications. The original IM had a rated power of 1.1 kW at a speed of 1437 rev/min (i.e., a rated torque of 7.3 Nm). First, the stator geometry of the original motor was measured, and a CAD model was built to redesign the rotors. A cut-section of the IM is shown in Fig. 1 and the main parameters are listed in Table I. Only the rotor was redesigned, while the stator, the winding arrangement, and the self-ventilation cooling apparatus remain the same as the starting IM.

The design procedure adopted in this paper consists of three main steps:

1. First, the number of barriers, their position, and shape were optimized for maximum torque per ampere and minimum torque ripple. This is called the initial SyR machine design.
2. The PM contribution was designed using a fictitious magnet filling the barriers, whose remanence was calibrated to meet the PM-assistance requirements.
3. Finally, the shape of the barriers was adapted to accommodate commercial magnet pieces, thus reducing the manufacturing cost.

The proposed 3-step procedure produces a design with maximized torque per Ampere (below base speed), and the required output power at maximum speed, with the minimum possible quantity of magnet. The downside of this easy-to-implement procedure is that torque ripple of the final PM-SyR machine design is no longer minimized. The torque ripple optimization of the initial SyR machine design is partially lost after PM insertion, and requires dedicated actions such as rotor skewing or local optimization of the barrier ends positions, including asymmetric pole solutions.

A. Optimization of Rotor Flux Barriers

The performance of a SyR motor is mainly related to the achievable magnetic saliency, which in turn is determined by the rotor lamination geometry. In particular, key elements in the rotor design are the number of flux barrier per pole (referred to as layers in the following), the angular position of each layer on the rotor periphery with respect to the magnetic q-axis of the pole ($\Delta\alpha_i$), and the barrier thickness (h_{ci}). These parameters are graphically defined in Fig. 2. Different rotor barrier shapes and numbers of barriers per pole were considered, eventually leading to a rotor with three barriers per pole coupled with the original 36-slots, 4-pole IM stator.



Fig. 1. Cut-section of the commercial induction motor stator.

TABLE I
INDUCTION MOTOR MAIN PARAMETERS

Item	Unit	Value
Rated power	kW	1.1
Rated speed	rpm	1437
Rated torque	Nm	7.3
Rated voltage	V	400
Rated current	A	2.3
Rtator diameter	mm	150.0
Rotor diameter	mm	91.4
Air-gap length	mm	0.35
Axial length	mm	100.5
Number of slots		36
Winding type		Single-layer
Number of turns per coil		52

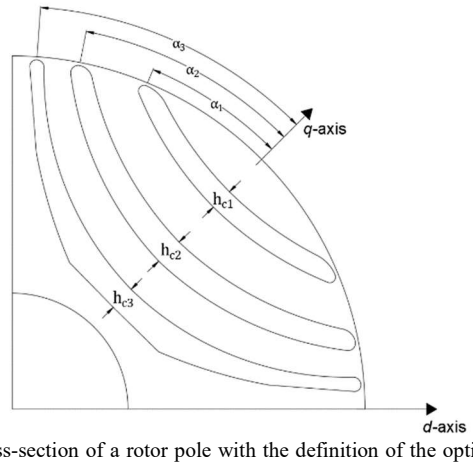


Fig. 2. Cross-section of a rotor pole with the definition of the optimization variables for barrier design.

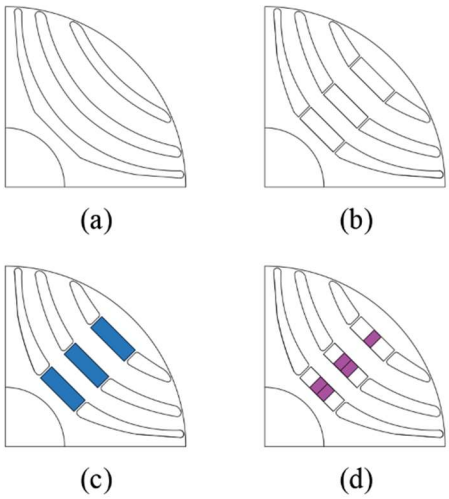


Fig. 3. Cross-section of a rotor pole: a) original barriers, b) modified barriers to accommodate the magnets, c) modified barriers with ferrite magnets, and d) modified barriers with NdFeB magnets.

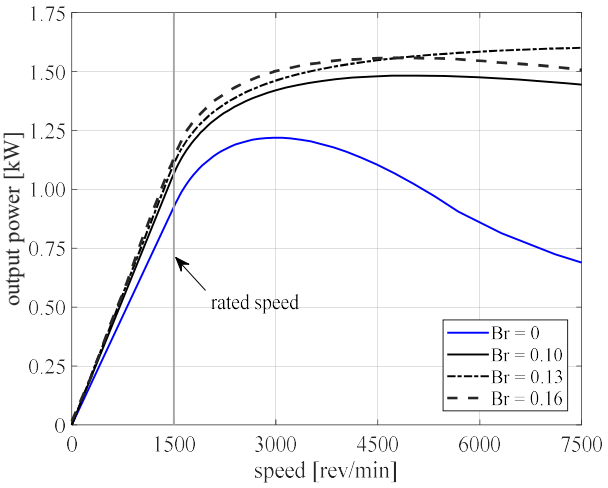


Fig. 4. Power vs. speed profiles for the selection of magnet fictitious remancence.

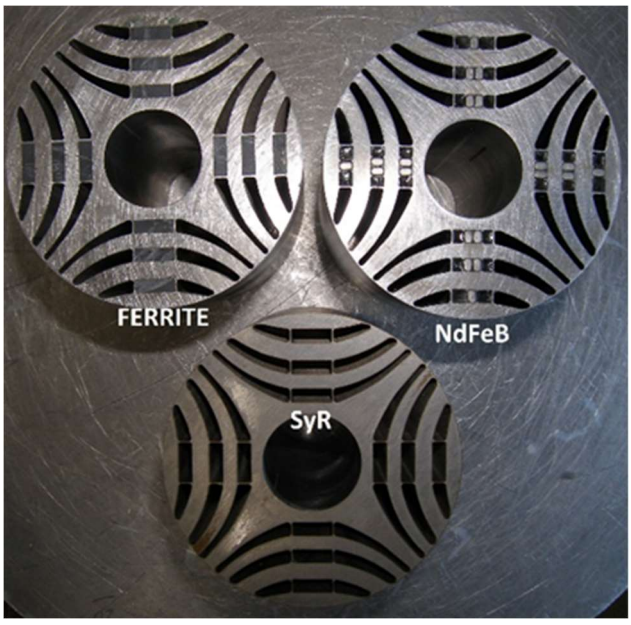


Fig. 5. Picture of the three prototype rotors assembled.

The shape of the barriers follows the field lines in a solid rotor, using the conformal mapping theory, as suggested in [19]. The design was aided by the multi-objective optimization algorithm to pursue the best compromise between average torque and torque ripple. Finite element analysis (FEA) was used during the optimization [20-21]. More details on the design steps can be also found in [6]. The optimized SyR rotor, which has been verified for mechanical robustness, is reported in Fig. 3a and referred to as the one with "original rotor layers."

B. Permanent Magnet Design

The second design step deals with the selection of the PM quantity and geometry. For the sake of simplicity, the barriers were initially assumed to be completely filled with a magnet material having fictitious remanence B_r' and parallel magnetization direction. B_r' is used as a design parameter to fine-tune the power vs. speed profile of the machine, targeting a high constant-power speed range with constrained maximum voltage and current. Fig. 4 shows the power characteristic of the machine for different values of B_r' in the same rotor laminations, namely the original rotor layers, under voltage and current constraints. The best constant-power speed range is obtained with $B_r' = 0.13\ T$: in fact, an increase of magnet strength would lead to a power drop at maximum speed. Therefore, the condition $B_r' = 0.13\ T$ was selected for the design and used for determining the final shape and volume of both the ferrite and neodymium magnets. The simulations are carried out considering a linear PM characteristic defined by the values of the remanence B_r' and the relative permeability μ_r.

C. Magnets Replacement Principle

Unless cast-bonded magnets are used, the solution discussed above is hardly manufacturable. To obtain the same result with much lower manufacturing complexity and cost, the $B_r' = 0.13\ T$ magnets were replaced with smaller pieces of higher-strength magnetic material: namely, rectangular pieces of commercial ferrite or NdFeB magnets. Defining A_r' as the area of one barrier, and B_r as the remanence of the final magnet piece, the area of the new magnet, A_r, can be found by simple proportions:

$$A_r = A_r{}' \cdot \frac{B_r{}'}{B_r} \tag{1}$$

The output of the resulting PM-SyR machine is the same for a magnet of remanence B_r' and volume V_m' as it is for a magnet with remanence B_r and volume V_m.

D. Final Geometry of the three rotors

Following the magnet replacement principle (1), two PM-SyR rotors were built:

- one with ferrite BMHF-32/32 magnets ($B_r = 0.41\ T$);
- one with BMN-38H NdFeB magnets ($B_r = 1.22\ T$).

The original rotor layers were modified, as shown in Fig 3b, to realize rectangular pockets large enough to accommodate the PMs. Thin radial ribs were also added to each barrier to avoid magnet displacement with motion and to

improve mechanical robustness. Rib thickness was chosen equal to the minimum tolerance allowed by the laser cut technology adopted to realize the laminations. Three identical rotor stacks were manufactured according to the final geometry visible in Fig. 3b. Of the three stacks, one was left with no magnets; the other two were equipped with ferrite and neodymium PMs, obtaining the two PM-SyR rotors, as shown in Fig. 3c and Fig. 3d, respectively.

In principle, each layer would need a different quantity of magnet. However, to reduce cost and improve the manufacturability, both the PM-SyR prototypes were realized with equal magnet pieces for all three layers. The cross-section area of PM pieces is 12 x 4 mm^2 for the ferrite pieces, and 2.5 x 4 mm^2 for the NdFeB sections. The calculated optimal magnet quantities for each layer and the selected commercial magnet pieces are compared in Table II. To quantify the goodness of the approximation, a weighted average remanence (B_r^{wa}) was calculated as defined in (2).

$$B_r^{wa} = \frac{\sum_k^{n_{lay}} B_r \cdot A_{PM,k}}{\sum_k^{n_{lay}} A'_{r,k}} \quad (2)$$

where $n_{lay} = 3$ is the number of barriers per pole, $A_{PM,k}$ is the selected magnet area within the k-th layer, and $A'_{r,k}$ is the area of the k-th barrier. With respect to the optimal remanence of 0.13 T, the error is 0.7% and 4% for the ferrite and NdFeB, respectively. Fig. 5 shows a picture of the three stacks assembled.

TABLE II
SELECTION OF OPTIMAL MAGNET DIMENSIONS

Layer	Layer area (mm^2)	Area of Ferrite magnets (mm^2)		Area of NdFeB magnets (mm^2)	
		Optimal	Selected	Optimal	Selected
Outer	95.24	30.95	48	10.15	10
Medium	173.65	56.44	48	18.30	20 (2x10)
Inner	182.13	59.19	48	19.41	20 (2x10)
		$B_r^{wa} = 0.1309\ T$ (+0.7%)		$B_r^{wa} = 0.1354\ T$ (+4.0%)	

III. TORQUE CAPABILITY AND DEMAGNETIZATION

Torque versus current loading capability of the three machines is comparatively shown in Fig. 6. The torque on current constant K_T is reported, from FEA and experiments, in maximum torque per ampere (MTPA) conditions. Fig. 6a reports the results in the current range up to 40 A, using experimental results up to 8A and simulation results for higher currents. Fig. 6b focuses on the low current range, up to 8A, comparing both simulation and experimental results. As expected, the two PM-SyR machines have a higher torque factor (i.e., absorb a lower current than the SyR machine for the same torque). At the rated points indicated in Fig. 6, each machine develops the rated torque, defined as the nameplate torque of the original IM.

Although both PM-assisted motors were designed to give the same torque at the same current level (namely 8 Nm at 3.6 A, peak value; i.e., 2.22 Nm/A), they perform similarly only up to the rated point. At overload condition, in fact, the characteristic of the Neo-SyR tends to go earlier into iron saturation, as pointed out in [14]. The main parameters of the three considered prototypes are reported in Table II.

A. Magnetic Analysis

This difference is also evidenced by the flux linkage curves of the three machines. Fig. 7 shows a comparison between the d-axis fluxes of the three machines as a function of the d-axis current. The curves refer to zero q-axis current conditions.

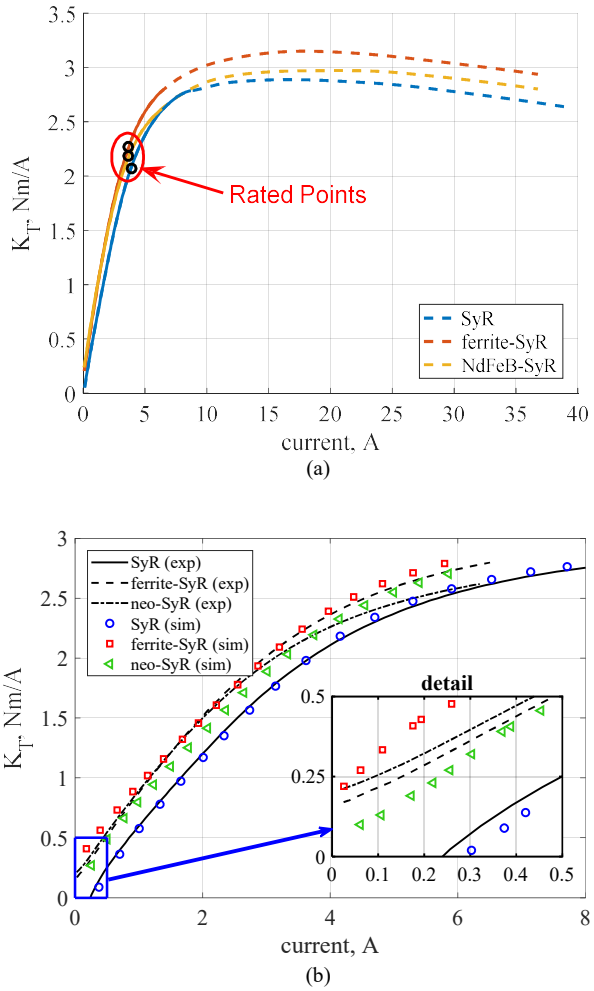


Fig. 6. Torque constant K_T as a function of current (peak values) for the three machines under study: continuous lines are experimental data, dashed lines are simulation results. Top figure (a) reports the current range up to 40A, bottom figures compares simulation and experimental results up to 8A.

TABLE III
MAIN PERFORMANCE FIGURES OF THE PROTOTYPES

	Unit	Value		
		SyR	Ferrite-SyR	Neo-SyR
Output power	kW		1.1	
Speed (rated/maximum)	rev/min		1500/5000	
Rated Torque	Nm		7.3	
Current (@7.3 Nm)	A_{rms}	2.59	2.39	2.45
Torque (@2.3 A_{rms})	Nm	5.96	6.88	6.65
Power factor	--	0.63	0.71	0.70

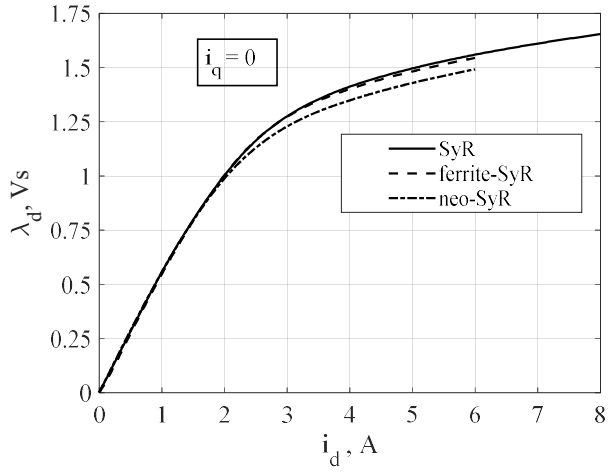


Fig. 7. Comparison of the d-axis flux linkage limit curves of the three prototypes.

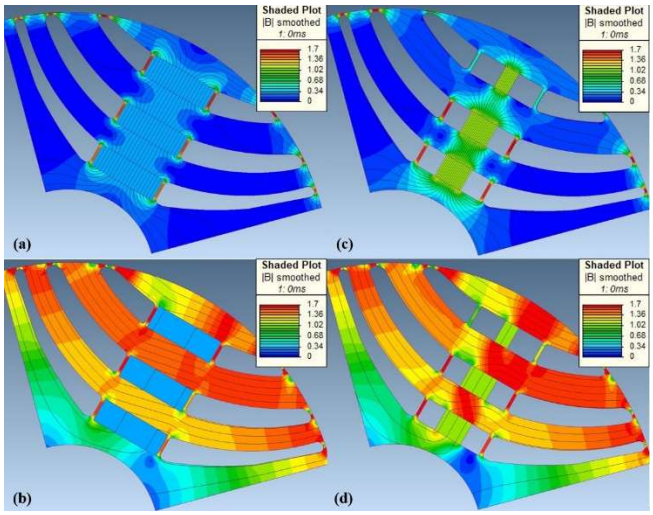


Fig. 8. Shaded plot of the magnetic flux density in the rotor of the two PM-SyR motors, at no load and rated d-axis current: a) ferrite, no load; b) ferrite, rated i_d; c) neodymium, no load; d) neodymium, rated i_d. The flux density range in the coloured map is from 0 to 1.7 T.

As can be seen, the curves of the SyR and ferrite-SyR motors behave similarly, while the neodymium-assisted motor goes earlier into iron saturation, showing a lower flux level in saturation. To understand the cause of this phenomenon, the FEA flux density distributions of the two rotors are compared (Fig. 8). Looking at the magnetic condition at no load, shown in Figs. 8a and 8c, the ferrite magnet allows a more uniform distribution of rotor flux, in particular inside the ribs that appear equally saturated. The stronger neodymium magnets lead to some local saturation along the rotor flux paths. Figs. 8b and 8d show the magnetic condition in the rotor when the rated current is applied along the d-axis only. It is evident in this case that local saturation phenomena occur within the space between the barriers when neodymium magnets are used due to their higher energy density.

B. Transient Overload Analysis

The transient overload capability of the three machines has limiting factors: 1) the maximum temperatures that the different parts can tolerate; and 2) the risk of magnet demagnetization. Commercial motors for general-purpose application are commonly manufactured with class F winding insulation, having a maximum admissible temperature of 155°C. Since the SyR motor has no magnets, and the selected ferrite PMs can tolerate up to 250°C, the temperature limit of the windings was considered as the maximum admissible temperature for the analysis. Conversely, the selected neodymium magnets present a maximum operating temperature of 120°C. Therefore, this value was used as the rotor temperature limit for the Neo-SyR motor.

C. Demagnetization limits

FEA was used to investigate the irreversible demagnetization limits for the PM-SyR machines within the admissible operating temperature range of the magnets (i.e., up to 250°C for the ferrite, and up to 150°C for the neodymium), with the stator current opposed to the direction of the PMs [22]. To obtain reliable results, the demagnetization curves of the PMs according to the manufacturer data sheets were implemented in Infolytica MagNet software [23].

Fig. 9 presents the results in the current vs. temperature plane. The temperature range was restricted to the range from -40°C to +120°C to improve readability. The percentage of demagnetized volume was calculated by discretizing each magnet with a mesh of squared elements (0.1x0.1 mm size) and analyzing the field value in each element. For each element, the demagnetization state was evaluated according to the position of the knee on the demagnetization curve at the simulated temperature. Finally, the percentage of demagnetized volume was calculated as the ratio of the number of demagnetized domains to the total number of elements. Fig. 9 reports, for each temperature, the current level at which 30% of the magnet volume is demagnetized. The ferrite-SyR machine is less robust toward demagnetization than the Neo-SyR machine, with a current limit of approximately 6 p.u. at 40°C vs. more than 12 p.u. of the Neo-SyR at the same temperature. However, a higher operating temperature is beneficial for the ferrite-SyR, while it degrades the robustness of the Neo-SyR machine.

A third case was included in this study: a Neo-SyR having the same magnet area of the manufactured machine but thinner length in the radial direction. A cross-section of this geometry is depicted in Fig. 10, while the results of the demagnetization study are shown in Fig. 9 and referred to as *"modified geometry."* By reducing the PM thickness, the magnets become easier to demagnetize at higher temperatures, even if the local saturation phenomena evidenced in the previous section for the manufactured neodymium rotor are slightly reduced, as evidenced by a comparison of Fig. 11 with Fig. 8d.

IV. THERMAL OVERLOAD LIMITS

In this section, the transient overload capability of the three machines is explored using MotorCAD [18]. Thermal limits of the machine active parts (copper and magnets) are considered, and demagnetization limits are included in the analysis, giving a general overview of the problem.

A. *Thermal Model Calibration*

Fig. 12 shows the ferrite-SyR machine model in MotorCAD. The shape of the flux barriers is slightly different from the original machine because of the rotor parametrization of the software. The stator and case geometries and the position of the magnets are accurately modeled, allowing a good modeling of the thermal behaviors. The model validation is performed by comparing the heating curve measured in the laboratory tests with the simulation results. The model is validated only for one machine (the ferrite-SyR) for sake of brevity.

During the heating test, the machine, supplied with constant *dq*-currents, runs at constant speed. Resistance at zero speed and voltage at no load were measured at regular time steps to estimate the average temperatures of the copper and magnets. The PM temperature was estimated from the PM flux linkage λ_{PM} measured at no-load. At the beginning of the test, when the PMs were at ambient temperature, T_0, the PM flux linkage $\lambda_{PM,0}$ was first measured. Then, the average PM temperature T_{PM} was estimated as

$$T_{PM} = T_0 + \frac{1}{\alpha_{PM}} \frac{\lambda_{PM}}{\lambda_{PM,0}} \tag{3}$$

where α_{PM} is the temperature coefficient of the magnet given by the manufacturer. Three tests were performed at 1500 rpm and different current levels (3.07 A, 3.67 A, and 5.52 A) along the MTPA. Fig. 13 compares the experimental measurements with the simulation results. The model results match the measurements with a good approximation: the maximum discrepancy is approximately 4°C.

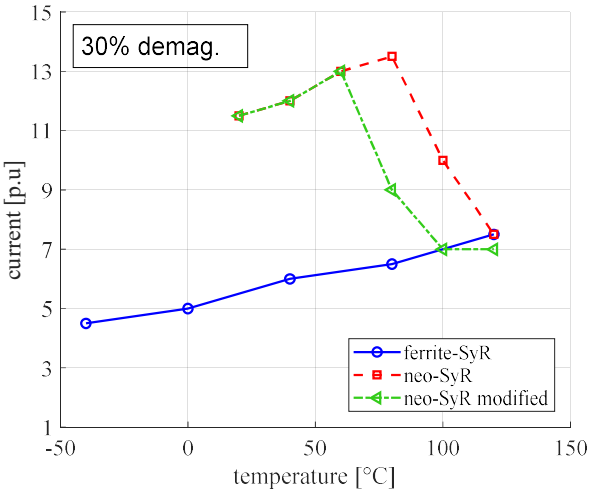


Fig. 9. Demagnetization of permanent magnets for ferrite-SyR (rotor in Fig.3c), Neo-SyR (rotor in Fig.3d), and Neo-SyR with modified geometry (rotor in Fig.10).

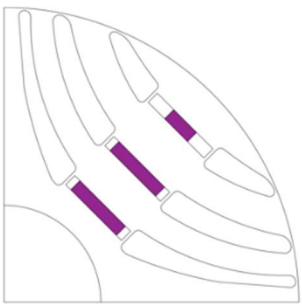


Fig. 10. Rotor cross-section of Neo-SyR with thinner magnets.

B. *Overload Limits*

The overload capability is defined as the maximum current that the machine can absorb for a certain time without exceeding the thermal limits of the materials. For the machines under analysis, the thermal limits are 155°C for the copper, 250°C for the ferrite PMs, and 150°C for the neodymium PMs. The overload current primarily depends on two parameters: the overload time and the ambient temperature. The longer the overload time, the closer the allowed current will be to the rated current value. Conversely, if the overload lasts for short periods, the allowed losses and current will be higher.

Figs. 14a, 15a, and 16a show the overload and demagnetization current curves for the SyR, ferrite-SyR, and Neo-SyR machines, respectively, expressed in per-unit of the rated current. Figs. 14b, 15b, and 16b, report the corresponding temperature values, reached by the copper (in red) and the PMs (in blue) at each overload condition (all temperatures represent final values of a thermal transient). The machine speed is set to 1500 rpm, and the ambient temperature is equal to 40 °C.

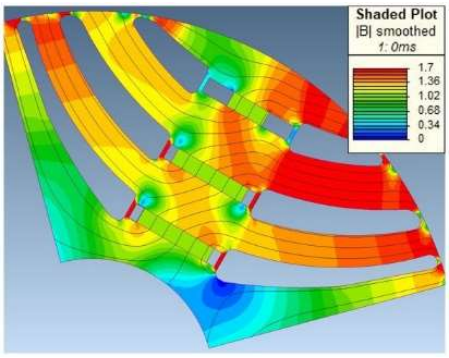


Fig. 11. Shaded plot of the magnetic flux density in the rotor of the Neo-SyR with thinner magnets at rated d-axis current. The flux density range in the coloured map is from 0 to 1.7 T.

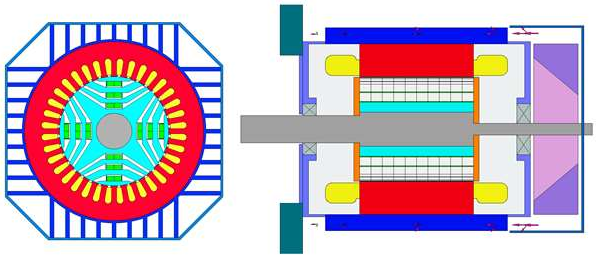


Fig. 12. Thermal model of the ferrite-SyR in MotorCAD.

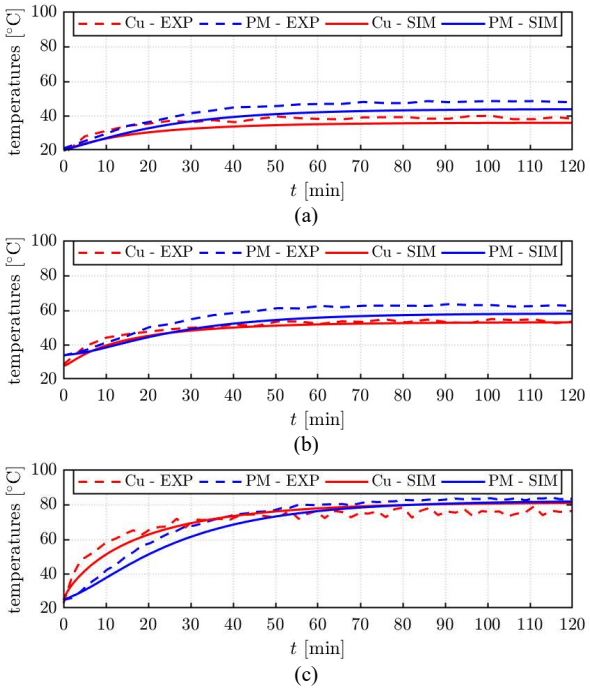


Fig. 13. Comparison of the measured (dashed lines) and simulated (full lines) temperatures during the load test: (a) 84% rated current; (b) 100%; and (c) 150%. Copper temperatures are reported in red, and PMs temperatures are reported in blue.

The overload curve of the SyR machine (Fig. 14a) shows that the SyR machine current limit is five times the nominal for two minutes; that is the time needed to increase the copper temperature from 40°C to 150°C. This overload curve is reported in the plots of the other two machines as a reference (Thermal limit SyR, in black). For the SyR machine, the continuous current that can be tolerated within thermal limits for continuous operation is about two times the rated current value. This is a common situation in high-efficiency motors.

The thermal limit curve of the ferrite-SyR machine (Fig. 15) is the same as that of the SyR machine because the magnet temperature is well below its limit (i.e. 250°C, dashed blue line). Therefore, the copper temperature is the only thermal constraint for the ferrite-SyR machine as well. Concerning the demagnetization limit (blue curve in Fig. 15a), it was defined calculating the current level that at steady state magnet temperature during overload condition demagnetize the magnets according to the analysis described in the previous section. The demagnetization limit is always above the thermal limit for ferrite-SyR machine. For short duration overload (e.g., 2 minutes, current equal to 5 per-unit), the demagnetization and thermal limits are close to each other, suggesting that a transient overload current of 5 per-unit is a safe upper limit for this machine, and is considered the demagnetization limit. It must be noted that when the ambient temperature is lower than 40°C, the ferrite magnets tend to suffer demagnetization issues. For example, at 0°C ambient, the demagnetization limit is exactly equal to 5 times the nameplate current.

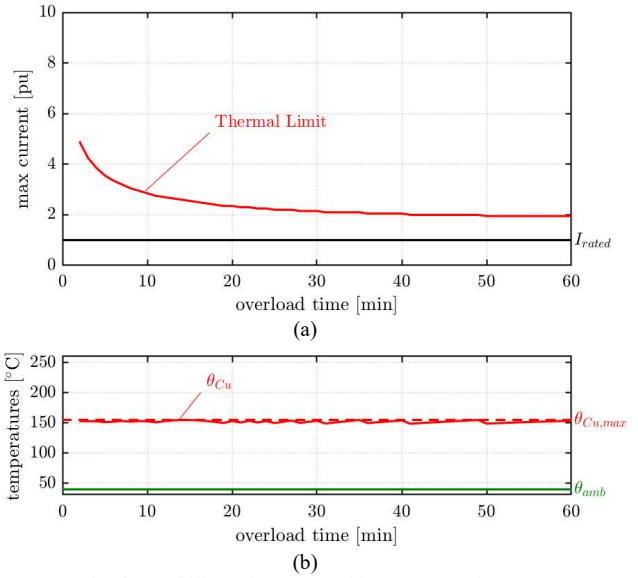


Fig. 14. Overload capability of SyR machine: (a) Maximum current vs. overload duration; and (b) and maximum copper temperature along the overload curve.

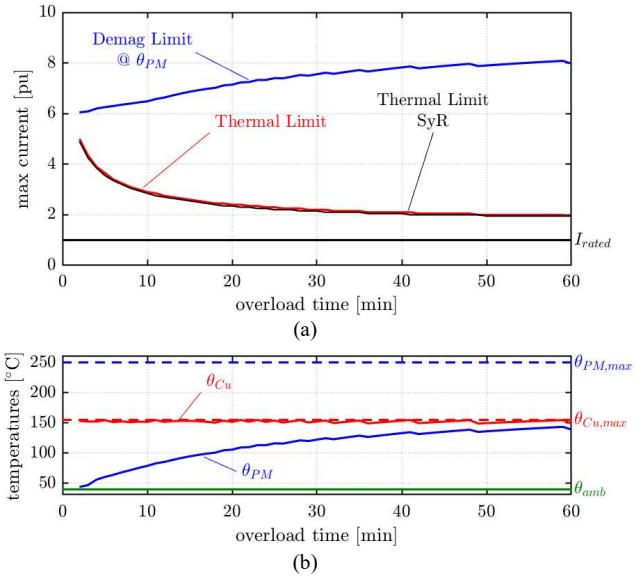


Fig. 15. Overload capability of the ferrite-SyR machine: (a) maximum current vs. overload duration and demagnetization limit; and (b) maximum copper and magnet temperature along the overload curve.

The thermal limit of the Neo-SyR machine is equal to that of the SyR machine for short overload times, below 25 minutes. However, for longer times, the PM temperature reaches its 120°C limit, and the current must be further limited, with respect to the value dictated by the copper constraints. The continuous current limit of this machine is about 1.5 p.u. and is lower than that of the previous two cases.

The demagnetization limit of the neodymium-assisted machine is high due to its high coercivity. For short time values, the blue curve of Fig. 16a is out of figure limits, whereas for longer times it is visible in the plot because of the higher magnet temperature. This machine can be overloaded for short periods at more than ten times its nominal current without demagnetization issues.

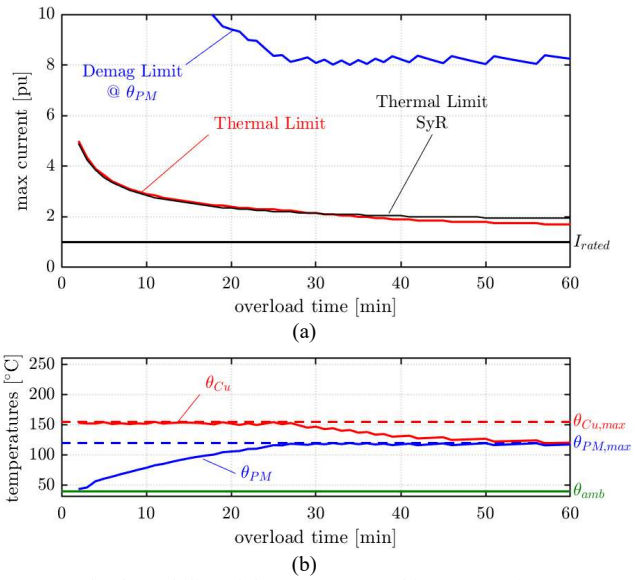


Fig. 16. Overload capability of the Neo-SyR machine: (a) maximum current vs. overload duration and demagnetization limit; and (b) maximum copper and magnet temperatures along the overload curve.

V. SENSORLESS CONTROL CAPABILITY

The abundant saliency of SyR machines can be profitably used for the sensorless estimation of the rotor position at low- and zero-speed operation. High-frequency (HF) voltage injection is often used to inspect the machine saliency and determine the rotor position and speed. Different approaches have been proposed, but in most of them the response of the machine to the HF excitation signal is demodulated and used in a position tracking loop. As an example, Fig. 17 reports the block diagram of one possible position observer [17], based on pulsating HF voltage injected into the machine estimated d-axis $\hat{d}$ (maximum permeance axis) and demodulation of the HF component of a current manipulation on the orthogonal axis.

SyR and PM-SyR machines offer a good level of magnetic anisotropy, in comparison to the other types of synchronous machines. Therefore, they are inherently suitable for zero-speed sensorless control based on signal injection. However, rotor saliency may vary with the operating point in the *(d,q)* current plane due to magnetic saturation, leading to sensitivity to the operating point and possible loss of information in certain operating conditions. Such phenomenon was studied in [15] for internal PM motors. In addition, the SyR motor presents specific issues in the low-current region, which are solved by PM-assisted machines. To clarify this, the key equations describing the machine response to alternating HF voltage signals are reported so to evidence the impact of the machine's parameters on sensorless control capability. The injected voltage in the estimated reference frame is shown in (4).

$$\begin{cases} v_{\hat{d}HF} = u_c \cdot \cos(\omega_c t) \\ v_{\hat{q}HF} = 0 \end{cases} \tag{4}$$

The $\hat{q}$ component of the current vector contains information about the rotor position error $\tilde{\theta} = \theta - \hat{\theta}$ signal and can be used to feed the tracking loop:

$$i_{\hat{q}HF} = \frac{u_c \sin(\omega_c t)}{2\omega_c\left(l_d l_q - l_{dq}^2\right)}\left[\left(l_d - l_q\right) sin\left(2\tilde{\theta}\right) - 2l_{dq}\, cos\left(2\tilde{\theta}\right)\right] \tag{5}$$

where l_d, l_q, and l_{dq} are the incremental inductances of the machine. If the position error is small ($\tilde{\theta} \approx 0$), and the second term of the difference in the square brackets is neglected, the demodulated signal $i_{\hat{q}HF,dem}$ obtained from (5) can be approximated by (6).

$$i_{\hat{q}HF,dem} \cong \frac{1}{2} k_\epsilon(i_d, i_q)\, sin\left(2\tilde{\theta}\right) \cong k_\epsilon(i_d, i_q) \cdot \tilde{\theta} \tag{6}$$

The parameter k_ϵ is a function of the incremental inductances of the machine, and ultimately, of the state of excitation of the machine defined by i_d, i_q:

$$k_\epsilon(i_d, i_q) = \frac{u_c\left(l_d - l_q\right)}{2\omega_c\left(l_d l_q - l_{dq}^2\right)} \tag{7}$$

This technique is widely used in literature for PM motors, characterized by low cross-saturation effect [16]. For highly salient machines the term $2l_{dq}\, cos\left(2\tilde{\theta}\right)$ neglected in (5) will produce a position estimation error due to cross-saturation. This error can be overcome if the $\hat{q}$ component of the estimated flux is demodulated in place of the current component, as in [17]. In this case, the error amplitude factor k'_ϵ (see Fig. 19) becomes, without approximations:

$$k'_\epsilon\left(i_d, i_q\right) = \frac{u_c}{2\omega_c} \cdot \frac{l_q\left(l_d - l_q\right) - 2l_{dq}^2}{l_d l_q - l_{dq}^2} \tag{8}$$

In the case of rotating voltage signal injection in the stationary $\alpha\beta$ reference frame, the injected HF signal can be expressed in complex notation as:

$$v_{\alpha\beta HF} = u_c \cdot e^{j\omega_c t} \tag{9}$$

Current response to this signal is an ellipse made of a rotating positive sequence component I_{pos}, plus a counter-rotating, negative sequence component I_{neg}:

$$i_{\alpha\beta HF} = I_{pos} \cdot e^{\left(j\omega_c t - \frac{\pi}{2}\right)} + I_{neg} \cdot e^{-j\left(\omega_c t - 2\theta - \varepsilon_{dq} + \frac{\pi}{2}\right)} \tag{10}$$

where $\varepsilon_{dq} = tg^{-1}\left(2l_{dq}/\left(l_q + l_d\right)\right)$. The argument of the negative sequence current component contains the rotor position θ plus the angular deviation due to cross saturation ε_{dq}. The amplitude I_{neg} is a function of the operating point:

$$I_{neg} = \frac{u_c\sqrt{\left(l_d - l_q\right)^2 + 4l_{dq}^2}}{2 \cdot \omega_c\left(l_d l_q - l_{dq}^2\right)}. \tag{11}$$

Neglecting the term $4l_{dq}^2$, which is small compared to $\left(l_d - l_q\right)^2$, the amplitude of the current I_{neg} becomes equal to $k_\epsilon\left(i_d, i_q\right)$ calculated for pulsating voltage injection. For this reason, a high value of k_ϵ corresponds to good sensorless control capability at low speed, regardless of the adoption of a pulsating or rotating voltage injection. It must be noted that the term $4l_{dq}^2$ is neglected here only to compare the pulsating and rotating HF voltage injection, summarizing the saliency information in a single parameter k_ϵ. An accurate sensorless control of SyR motors must consider cross-saturation.

A. *Saliency Analysis and Inspection*

A dedicated experimental test was performed to investigate the machine saliency in the whole *(d,q)* current plane. Each motor under test was kept at stand-still, and fundamental i_d and i_q were imposed to define the operating point under investigation. A HF rotating voltage was superimposed to the fundamental voltage signals at the output of current PI regulators and the current response was analyzed (Fig. 18). In an isotropic machine, such rotating voltage would produce a corresponding circular current trajectory in the dq plane. Conversely, in case of salient machine with $l_d \neq l_q$, the current response follows an ellipse. The higher is the saliency, the sharper is the ellipse. Therefore, for each working point, the ratio between the maximum and minimum axes gives visual representation of the machine saliency and its sensitivity to operating point variation. Without considering the effect of cross-saturation, the ellipse would be oriented the major axis in the direction of minimum inductance (i.e. l_q, vertical axis). The presence of l_{dq}≠0 deviates the major axis of the ellipse from the vertical axis. Such effect is particularly visible in the area with high i_d and high i_q. If not properly considered, this deviation produces steady state position error in saliency-based sensorless control, where the tracking loop converges to the direction of maximum inductance, i.e. the minor axis of the ellipse instead of the d axis. The physical explanation and position error quantification are reported in detail in [15].

Neglecting manufacturing asymmetries, results can be considered to be independent of rotor position since the *(d,q)* reference frame is employed. Results in Fig. 18 refer to the SyR and to the Neo-SyR motors, for comparison purposes. In this test, the ferrite-SyR motor presented very similar behavior to the Neo-SyR, so it is not reported for clarity purposes. The two machines present similar saliency characteristic and optimal sensorless control capability in most of the *(d,q)* current plane. The problem of SyR motors is that the saliency drastically drops in the area highlighted in the red rectangle, with i_q close to zero. Therefore, the sensorless position estimation can be armed and eventually fail at no load. This issue is inherently solved in the PM-SyR machine, which maintains a reasonable level of saliency even at no load, as further detailed in the next section.

Similar conclusions can be found when the gain k'_ϵ is analyzed in the (i_d, i_q) plane. In Fig. 19, the k'_ϵ parameter was computed using (8) and based on the experimentally measured flux-current characteristics. SyR and Neo-SyR motors are compared. Sensorless control is theoretically possible if the machine presents saliency, even if it is minimal, and in the correct direction (i.e., $k'_\epsilon > 0$). However, the smaller the saliency, the more difficult it is to track, so the position tracking loop may not converge or may converge to an incorrect position. In other words, the control is more sensitive to parameter uncertainty, such as stator resistance variation, inaccurate flux maps, imperfect compensation of inverter non-linearities, and uncertainty in current measurement. Therefore, a high value of k'_ϵ corresponds to high signal-to-noise ration while negative k'_ϵ leads to instability. As it can be seen, for the SyR machine the area in the red rectangle of Fig. 19, corresponding to low i_q, is critical since k'_ϵ drops. The addition of the magnets in the PM-SyR machine shifts the critical region to negative i_q values, avoiding lack of position information around the origin of the i_d, i_q plane (i.e. around zero current, zero torque conditions).

B. *Effect of Bridge Saturation*

The effects described above can be explained by considering the rotor structure of the two machines. If i_q is low and there are no magnets, the structural ribs are not saturated and therefore the flux crosses the rotor as if there were no flux barriers. In other words, under those circumstances, the reluctance in the q-axis is unexpectedly low and the same is true for the machine saliency. This phenomenon harms the stability of sensorless control of SyR at low speed in no-load conditions. The problem is overcome by imposing a minimum excitation current or flux to the machine. If sufficient current is given in the d-axis, the ribs tend to saturate because of the cross-saturation effect, thus leading the machine saliency to acceptable levels.

In the PM-assisted machines, the magnets have the precious function of saturating the ribs, also at zero current. This can be seen in the k'_ϵ map of Fig. 19b, where the critical area around zero q-axis current is shifted downwards, out of the operating quadrant. With PM-assistance, low-speed sensorless position estimation can be performed even at no-load without any need for a minimum flux excitation.

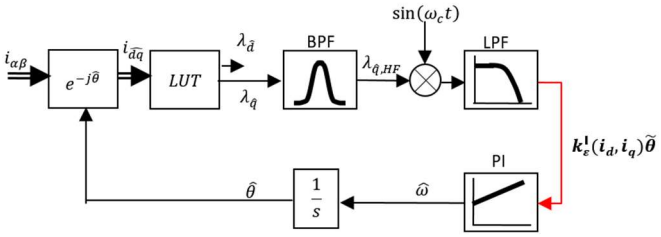


Fig. 17. Sensorless estimation of the rotor position using pulsating HF voltage injection. The key parameter kϵ(id,iq) is in evidence.

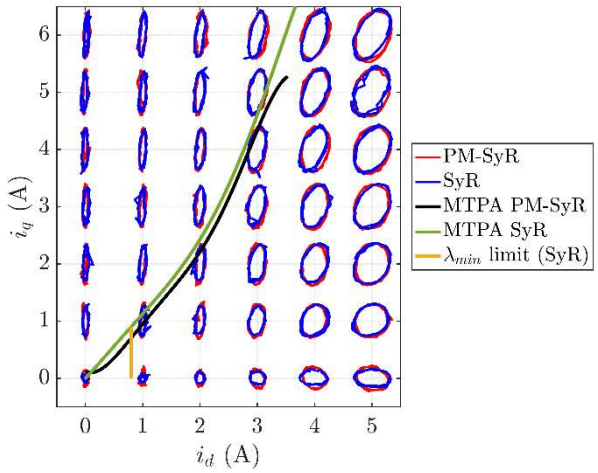
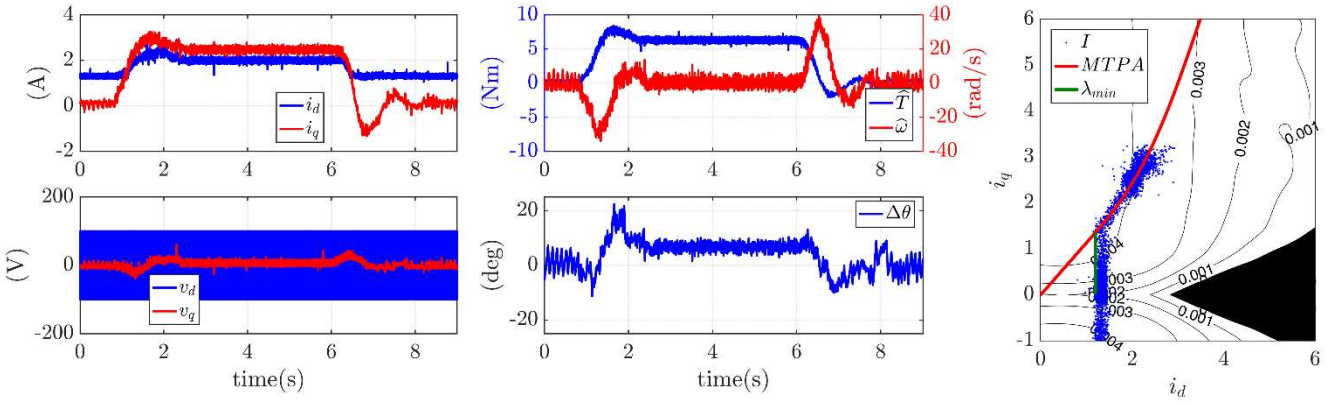
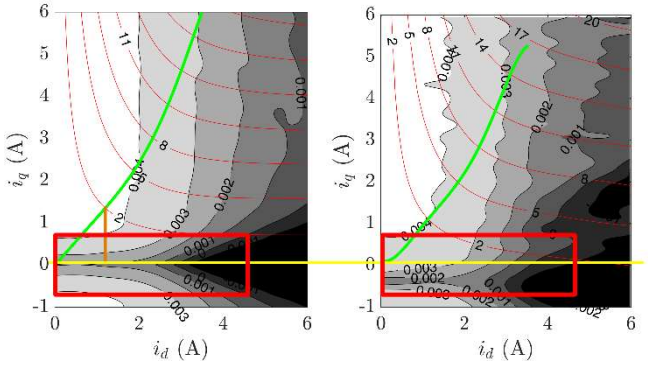


Fig. 18. Saliency analysis of SyR and Neo-SyR motors, experimental results.



(a) (b) (c)

Fig. 20. Sensorless speed control of the SyR motor. (a) currents and voltages in dq plane. (b) Estimated torque and speed and position error. (c) Movement of the current vector in the dq plane during the test. The shaded area is the unstable region for sensorless control.



(a) (b)

Fig. 19. The k'_ϵ contours: (a) SyR; and (b) Neo-SyR.

C. *Sensorless control implementation*

To better demonstrate the low-speed sensorless control feasibility, sensorless control was implemented for the SyR motor. The machine under test was in speed control with a reference speed $\omega^* = 0$, while a second drive was torque controlled to act as a load. A step torque of 7 N·m, equal to the rated value, was applied and removed. Fig. 20 reports the currents, voltages, observed speed, and torque and position error. As can be seen, the dynamic response is good, and the control is stable. Fig. 20c shows the movement of the current vector during the test along the minimum flux limit (low load) and on the MTPA (high load). It should be noted that The same test performed on one of the PM-SyR machines would be inherently more stable, since the PMs guarantee both ribs saturation (and therefore sufficient saliency) and minimum magnetic excitation at no load.

VI. Summary and Conclusions

This paper focuses on performance analysis of SyR and PM-SyR motors in overload conditions and on their sensorless control capability at zero speed. Three prototypes were realized to replace the rotor of a commercial high-efficiency IM, and tested. The adoption of PM-assisted solutions not only improves the efficiency and power factor but also enhances the magnetic saliency at low current levels, with advantages for sensorless position detection. It was demonstrated that the SyR motor assisted by ferrite magnets guarantees the best overload performances in terms of torque production capability thanks to the higher operating temperature of the ferrite magnets. Conversely, the SyR motors assisted by neodymium magnets are more robust toward demagnetization. Both considered PM-assisted solutions appear as viable alternatives to IMs to improve not only the efficiency but also the overload performances and sensorless control capability, with limited impact on cost.

References

[1] A. Boglietti, A. Cavagnino, M. Pastorelli, D. Staton and A. Vagati, "Thermal analysis of induction and synchronous reluctance motors," in IEEE Trans. Ind. Appl., vol. 42, no. 3, pp. 675-680, May-June, 2006.

[2] T. Matsuo and T. A. Lipo, "Rotor design optimization of synchronous reluctance machine," in IEEE Transactions on Energy Conversion, vol. 9, no. 2, pp. 359-365, Jun 1994.

[3] H. Hofmann and S. R. Sanders, "High-speed synchronous reluctance machine with minimized rotor losses," in IEEE Transactions on Industry Applications, vol. 36, no. 2, pp. 531-539, Mar/Apr 2000.

[4] W. L. Soong and T. J. E. Miller, "Field-weakening performance of brushless synchronous AC motor drives," in IEE Proceedings - Electric Power Applications, vol. 141, no. 6, pp. 331-340, Nov 1994.

[5] A. Vagati, M. Pastorelli, G. Francheschini and S. C. Petrache, "Design of low-torque-ripple synchronous reluctance motors," in IEEE Transactions on Industry Applications, vol. 34, no. 4, pp. 758-765, Jul/Aug 1998.

[6] G. Pellegrino, F. Cupertino and C. Gerada, "Automatic Design of Synchronous Reluctance Motors Focusing on Barrier Shape Optimization," in IEEE Transactions on Industry Applications, vol. 51, no. 2, pp. 1465-1474, March-April 2015.

[7] N. Bianchi, E. Fornasiero and W. Soong, "Selection of PM Flux Linkage for Maximum Low-Speed Torque Rating in a PM-Assisted Synchronous Reluctance Machine," in IEEE Transactions on Industry Applications, vol. 51, no. 5, pp. 3600-3608, Sept.-Oct. 2015.

[8] S. Morimoto, M. Sanada and Y. Takeda, "Performance of PM-assisted synchronous reluctance motor for high-efficiency and wide constant-power operation," in IEEE Transactions on Industry Applications, vol. 37, no. 5, pp. 1234-1240, Sep/Oct 2001.

[9] R. Leuzzi; P. Cagnetta; S. Ferrari; P. Pescetto; G. Pellegrino; F. Cupertino, "Analysis of overload and sensorless control capability of PM-assisted synchronous reluctance machines", IEEE Workshop on Electrical Machines Design, Control and Diagnosis (WEMDCD), Nottingham (UK), 2017, pp. 172 – 178.

[10] G. Scarcella, G. Scelba and A. Testa, "High performance sensorless controls based on HF excitation: A viable solution for future AC motor drives?," 2015 IEEE Workshop on Electrical Machines Design, Control and Diagnosis (WEMDCD), Torino, 2015, pp. 178-187.

[11] M. Harke, H. Kim and R. D. Lorenz, “Sensorless control of interior permanent magnet machine drives for zero-phase-lag position estimation,” IEEE Transaction on Industry Applications, vol. 39, no. 12, pp. 1661-1667, Nov./Dec. 2003.
[12] N. Bianchi, S. Bolognani, J. H. Jang and S. K. Sul, "Comparison of PM Motor Structures and Sensorless Control Techniques for Zero-Speed Rotor Position Detection," in IEEE Transactions on Power Electronics, vol. 22, no. 6, pp. 2466-2475, Nov. 2007.
[13] A. Vagati, M. Pastorelli, F. Scapino and G. Franceschini, "Impact of cross saturation in synchronous reluctance motors of the transverse-laminated type," in IEEE Transactions on Industry Applications, vol. 36, no. 4, pp. 1039-1046, Jul/Aug 2000.
[14] R Leuzzi, P Cagnetta, F Cupertino, S Ferrari, G Pellegrino, “Performance assessment of ferrite-and neodymium assisted synchronous reluctance machines”, IEEE Energy Conversion Congress and Exposition (ECCE), 2017, Cincinnati OH (USA), pp. 3958-3965.
[15] N. Bianchi and S. Bolognani, "Influence of Rotor Geometry of an IPM Motor on Sensorless Control Feasibility," in IEEE Transactions on Industry Applications, vol. 43, no. 1, pp. 87-96, Jan.-feb. 2007.
[16] J. Holtz, “Acquisition of Position Error and Magnet Polarity for Sensorless Control of PM Synchronous Machines”, IEEE Transactions on Industry Applications, Vol. 44, n. 4, July-Aug. 2008 Page(s):1172 – 1180.
[17] A. Yousefi-Talouki; P. Pescetto; G. Pellegrino, "Sensorless Direct Flux Vector Control of Synchronous Reluctance Motors Including Standstill, MTPA and Flux Weakening," in *IEEE Transactions on Industry Applications*, vol. 53, no. 4, pp. 3598 – 3608, July-Aug. 2017.
[18] Motor Design Ltd, "MotorCAD" software
[19] RR Moghaddam, “Rotor for a Synchronous Reluctance Machine”, US Patent App. 13/230,543, 2011.
[20] David Meeker, “Finite Element Method Magnetics”, Ver. 4.2 User’s Manual, February 5, 2009, [Online] available: http://www.femm.info/Archives/doc/manual.pdf.
[21] Cupertino, F., Pellegrino, G.; “SyR-e - Synchronous Reluctance (machines) – evolution”, available at http://sourceforge.net
[22] K. C. Kim, K. Kim, H. J. Kim and J. Lee, "Demagnetization Analysis of Permanent Magnets According to Rotor Types of Interior Permanent Magnet Synchronous Motor," in IEEE Transactions on Magnetics, vol. 45, no. 6, pp. 2799-2802, June 2009.
[23] Infolytica. Available online: http://www.infolytica.com/
[24] M. Hirota, M. Sanada, S. Morimoto and Y. Inoue, "Improvement of rotor structure on irreversible demagnetization in double-layered IPMSM with Dy-less magnet," 2015 IEEE Energy Conversion Congress and Exposition (ECCE), Montreal, QC, 2015, pp. 1795-1802.
[25] N. Bianchi and H. Mahmoud, "An Analytical Approach to Design the PM in PMAREL Motors Robust Toward the Demagnetization," in IEEE Transactions on Energy Conversion, vol. 31, no. 2, pp. 800-809, June 2016.
[26] A. Vagati, B. Boazzo, P. Guglielmi and G. Pellegrino, "Design of Ferrite-Assisted Synchronous Reluctance Machines Robust Toward Demagnetization," in IEEE Transactions on Industry Applications, vol. 50, no. 3, pp. 1768-1779, May-June 2014.